Stem Cell Research & Therapy

RESEARCH

Open Access

Modeling pathogenesis and progression of metabolic dysfunction-associated steatotic liver disease and therapeutic drug screening using hESC-derived mature polarized hepatocyte organoids

Changlu Qin[1,2,3†], Haibin Wu[1,2,3†], Peilin Liao[2†], Wenjiao Yan[1,2,3], Xinyi Shi[1,2,3], Jinghe Xie[3,4], Shoupei Liu[1,2,3], Sen Chen[1,2,3], Xiangting Cao[1,2,3], Yongjian Zhou[1,8*] and Yuyou Duan[1,2,3,5,6,7*]

Abstract

Background Metabolic dysfunction-associated steatotic liver disease (MASLD), the most prevalent chronic liver disorder worldwide, exhibits complex pathogenesis and lacks effective targeted therapeutics. Existing animal models are limited by prolonged induction periods and interspecies discrepancies, while conventional monolayer hepatocyte cultures fail to recapitulate disease pathology due to inadequate polarization and functional immaturity.

Methods To overcome these limitations, we established an in vitro MASLD model by treating human embryonic stem cell (hESC)-derived mature polarized hepatocyte organoids (P-hep-orgs) with free fatty acids (FFAs). Pathogenesis and progression of MASLD in this model were characterized using multiple assays, and its utility for drug screening was validated with three known antioxidant or lipid-lowering agents.

Results P-hep-orgs derived from hESCs expressed mature hepatocyte markers (e.g., ALB), exhibited polarized architecture (e.g., MRP2) and demonstrated functionalities of mature hepatocytes (e.g., urea production). Moreover, we developed an in vitro MASLD model by treating P-hep-orgs with FFAs. This model recapitulated key pathological progression hallmarks, including disrupted glucose/lipid metabolism, oxidative stress, apoptosis, loss of polarization, impaired liver function, and ductular reaction. Furthermore, transcriptomic analysis revealed that P-hep-orgs treated with FFAs for 10 days shared similar molecular signatures with human MASH liver tissues (581 overlap DEGs). Finally, this model was used to assess the potential efficacy of established antioxidant or lipid-lowering agents (e.g., Vitamin E) in alleviating pathological phenotypes, including lipid accumulation and oxidative stress.

†Changlu Qin, Haibin Wu and Peilin Liao have contributed equally to this work.

*Correspondence:
Yongjian Zhou
yongjian_zhou@outlook.com
Yuyou Duan
yuyouduan@scut.edu.cn

Full list of author information is available at the end of the article

© The Author(s) 2025. **Open Access** This article is licensed under a Creative Commons Attribution-NonCommercial-NoDerivatives 4.0 International License, which permits any non-commercial use, sharing, distribution and reproduction in any medium or format, as long as you give appropriate credit to the original author(s) and the source, provide a link to the Creative Commons licence, and indicate if you modified the licensed material. You do not have permission under this licence to share adapted material derived from this article or parts of it. The images or other third party material in this article are included in the article's Creative Commons licence, unless indicated otherwise in a credit line to the material. If material is not included in the article's Creative Commons licence and your intended use is not permitted by statutory regulation or exceeds the permitted use, you will need to obtain permission directly from the copyright holder. To view a copy of this licence, visit http://creativecommons.org/licenses/by-nc-nd/4.0/.

Conclusions In summary, we established a novel in vitro MASLD model using hESC-derived P-hep-orgs. This model faithfully recapitulates key aspects of MASLD progression and serves as a valuable platform for investigating disease mechanisms and screening potential therapeutic compounds.

Keywords Metabolic dysfunction-associated steatotic liver disease, Human embryonic stem cells, Hepatocyte organoids, Polarized structure, Free fatty acids, Drug screening

Introduction

Metabolic dysfunction-associated steatotic liver disease (MASLD), formerly termed non-alcoholic fatty liver disease (NAFLD), represents the most prevalent chronic liver condition globally, affecting approximately 30% of the population [1]. As a leading etiology of liver-related morbidity and mortality, including the cirrhosis and hepatocellular carcinoma [2, 3], MASLD poses a significant clinical burden. Its pathogenesis involves multifactorial mechanisms [4], and there exists no specific drug currently [5, 6]. These challenges underscore the urgent need for physiologically relevant models that accurately recapitulate disease progression to facilitate mechanistic studies and therapeutic discovery. Current researches on MASLD predominantly employ animal models such as mice [7] and rats [8] to study MASLD, yet these studies suffer from protracted induction times, inter-batch variability, and interspecies physiological discrepancies [9]. While in vitro cell models mitigate some limitations of animal studies, conventional systems inadequately replicate the structural and functional complexity of human hepatocytes, hindering breakthrough research on MASLD.

Hepatocyte polarization underpins critical physiological functions, such as metabolism, secretion, and detoxification [10]. In vivo, hepatocytes establish two functional domains through the asymmetric distribution of membrane proteins (e.g., Na+/K+-ATPase, bile acid transporters), which demarcate the basolateral domain adjacent to hepatic sinusoids and the apical membrane domain facing bile canaliculi. This polarized configuration regulates the directional uptake and secretion of carbohydrates, lipids, and other molecules [11], thereby governing their absorption, transport, and metabolic pathways. The disruption of hepatocyte polarization induces abnormal lipid metabolism, thereby enhancing lipid toxicity to hepatocytes. Existing MASLD cell models rely primarily on either immortalized hepatocyte cell lines (e.g., HuH7, HepaRG) [12, 13] or two-dimensional (2D) hepatocytes derived from human pluripotent stem cells (hPSCs) [14, 15]. Alternatively, these hepatocytes are enzymatically dissociated into single-cell suspensions and cultured under low-adhesion conditions to spontaneously form non-structured hepatocyte aggregates [16]. These systems fail to reconstitute authentic polarization, limiting their capacity to model spatiotemporal disease dynamics. Although Transwell [17] and collagen sandwich [18] cultures partially restore the polarity in 2D culture, scalability remains constrained. While three-dimensional (3D) hepatocyte organoids better mimic in vivo microenvironments [19], current protocols exhibit critical limitations, including the dependence on high-concentration Matrigel [20, 21] or the generation of functionally immature hepatocytes [22, 23]. These shortcomings impeding the construction and scalable application of MASLD models based on 3D hepatocyte organoids.

Recently, our group developed a differentiation protocol that directs human embryonic stem cells (hESCs) into hepatoblast organoids (HB-orgs) supporting large-scale stable expansion under low-concentration Matrigel conditions [24]. These HB-orgs further could be maturated into polarized hepatocyte organoids (P-hep-orgs) under defined culture conditions [24]. Herein, we leveraged this platform to develop a novel MASLD model by treating P-hep-orgs with free fatty acids (FFAs), and this system recapitulated early (glucolipid dysregulation, oxidative stress) and advanced (hepatic dysfunction, apoptosis, polarization loss, ductular reaction) pathological features. Transcriptomic profiling was performed to reveal the alignment with patient livers of metabolic dysfunction-associated steatohepatitis (MASH). Finally, we demonstrated the model's utility of drug screening by testing three known antioxidant or lipid-lowering agents.

Materials and methods

Cell culture

Human embryonic stem cell (hESC) line, H9 cells used in this study was obtained from WiCell Institute under Material Transfer Agreements (MTAs) (19-W0512, 24-W0162, and 24-W0163). H9 cells were cultured on mouse embryonic fibroblast feeder layers in DMEM/F12 medium supplemented with 1% non-essential amino acids, 20% KnockOut Serum Replacement (KSR), 0.5% GlutaMAX, 0.1 mM β-mercaptoethanol, and 8 ng/mL bFGF at 37 °C under 5% CO_2. The medium was replaced daily. Cells were passaged at 80–90% confluency using 1 mg/mL collagenase IV solution and re-seeded onto fresh feeder layers. Catalog numbers and suppliers for all commercial reagents used in this study were provided in Supplementary Table 1.

Differentiation of definitive endoderm (DE) form hESCs

H9 cells at 60–70% confluency were treated with Gentle Cell Dissociation Reagent (GCDR) for 3 min at 37 °C.

Detached cells were resuspended in mTeSR1 medium containing 10 μM Y-27,632 and transferred to low-attachment 6-well plates. After 24 h, medium was replaced with mTeSR1 without Y-27,632. The differentiation of DE commenced when aggregates reached 100–200 μm in diameter, lasting 3 days with daily medium changes as the following, RPMI 1640 supplemented with 100 ng/mL Activin A and 3 μM CHIR99021 on days 0–1, RPMI 1640 with 100 ng/mL Activin A and 0.8% KSR on day 1–2, and RPMI 1640 with 100 ng/mL Activin A and 8% KSR on day 2–3. Morphological changes, including increased aggregate size, rounding, and edge smoothing, were monitored throughout the process.

Differentiation of hepatoblast (HB) spheres from hESC-derived DE

Following the differentiation of DE, medium was replaced with IMDM supplemented with 20% FBS, 1% GlutaMAX, 1% Penicillin-Streptomycin-Amphotericin B (PSA), 0.3 mM 1-thioglycerol, 100 nM dexamethasone, 0.126 U/mL human insulin, 20 ng/mL FGF-4, 10 ng/mL BMP2, 20 ng/mL HGF and 10 ng/mL BMP4. The medium was changed daily for 6 days to generate HB spheres.

Differentiation and expansion of hepatoblast organoids (HB-orgs)

HB spheres were dissociated into single cells using TrypLE at 37 °C, and cells were resuspended in HB-org expansion medium (IMDM with 10% FBS, 1% ITS-E, 1% GlutaMAX, 1% non-essential amino acids, 1% PSA, 10 mM nicotinamide, 5 μM CHIR99021, 10 μM SB431542, 10 μM forskolin, 20 ng/mL EGF, 20 ng/mL FGF-4, 10 ng/mL BMP-4, and 10 μM Y-27632 added on day 0/passaging) and seeded into low-attachment plates. 24 h after the culture, 5% Growth Factor Reduced (GFR) Matrigel was thawed on ice and supplemented directly into the culture medium, to provide an extracellular matrix (ECM) microenvironment supporting long-term culture of HB-orgs. The medium was replaced daily. Under these conditions, HB-orgs formed vacuole-like structures enabling sustained expansion. The passaging procedure for HB-orgs was identical to that of their differentiation, with the addition of 5% GFR-Matrigel at the start of passaging.

Maturation of polarized hepatocyte organoids (P-heporgs)

When HB-orgs reached a diameter of 100–200 μm, they were maturated in Hepatocyte Culture Medium (HCM) supplemented with 100 nM dexamethasone, 2% B-27, 20 ng/mL FGF-4, 20 ng/mL HGF, and 50 ng/mL Oncostatin M. The medium was changed every 48 h.

Reverse transcription quantitative polymerase chain reaction (RT-qPCR)

Total RNAs were extracted using RNAiso Plus kit following the manufacturer's instructions. RNAs were then reverse-transcribed into cDNA using reverse transcription kit. SYBR Green was used to prepare the reaction mixture for reverse transcription, and RT-qPCR was performed on real-time PCR instrument (Thermo, QUANTSTUDIO 5). Gene expression was normalized to housekeeping gene glyceraldehyde-3-phosphate dehydrogenase (GAPDH) and calculated using 2^(-ΔΔCt) method. Primer sequences were listed in Supplementary Table 2.

Immunofluorescence (IF) staining

Organoids were fixed in 4% paraformaldehyde (PFA) overnight at 4 °C, permeabilized with 0.5% Triton X-100 for 20 min, and blocked with goat serum or 5% BSA for 1 h. Primary antibodies were applied overnight at 4 °C. After warming to 37 °C for 1 h, samples were incubated with fluorophore-conjugated secondary antibodies for 1 h at room temperature (RT) in dark, followed by DAPI nuclear counterstaining for 5 min. Samples were washed with phosphate-buffered saline (PBS) solution for 3 times between steps. Images were acquired using a confocal microscope (ZEISS, LSM900) and processed with ZEN 2.3 software. Antibodies used were listed in Supplementary Table 3.

Glycogen storage capacity test

Glycogen storage capacity in P-hep-orgs was assessed using a Periodic Acid-Schiff (PAS) staining kit, in accordance with the manufacturer's instructions.

Detection of indocyanine green (ICG) uptake and excretion capacity

To assess ICG uptake, P-hep-orgs were incubated with 1 mg/mL ICG in the medium for 1 h at 37 °C under 5% CO_2 and then observed under a microscope. Subsequently, to evaluate ICG excretion, P-hep-orgs were gently rinsed three times with PBS, incubated in fresh medium for an additional hour, and then re-examined microscopically.

Quantitative detection of human albumin secretion levels

Conditioned medium was collected and diluted 20-fold for the detection of albumin (ALB). ALB concentration was quantified using human Albumin ELISA kit according to the manufacturer's protocol. The absorbance was measured at 450 nm using microplate reader (Thermo, Varioskan LUX). Concentrations were calculated against a standard curve using Origin software.

Urea production capacity test

Organoids were incubated with 10 mM ammonium chloride in culture medium for 24 h. Following this, culture medium was collected, and urea concentration in the medium was measured using a Urea Nitrogen Detection Kit according to the manufacturer's instructions.

Induction and detection of CYP450 drug metabolism capacity

Organoids were treated with 25 μM rifampicin and 100 μM omeprazole respectively in culture medium for 48 h to induce the expression of CYPs. The mRNA expression levels of CYP family genes were then analyzed by RT-qPCR.

Development of model of MASLD using P-heporgs

Oleic acid (OA) solution (100 mM in DMSO) and palmitic acid (PA) solution (100 mM in ethanol) were added to P-heporg culture medium at 2:1 (OA: PA) ratio. The duration of the treatment was varied based on experimental requirements.

Cell viability assay

The viability was assessed using Cell Counting Kit-8 (CCK-8), and the absorbance was measured at 450 nm. Cell survival rate was calculated relative to untreated controls.

Triglyceride (TG) measurement

Organoids were washed with PBS, resuspended in 200 μL PBS, and sonicated on ice (15 W, 5 s pulse/5 sec interval, 10 cycles). Lysates were analyzed using TG assay kit (absorbance at 500 nm). Data were normalized to total protein concentration.

Glucose measurement

Organoids and conditioned medium were collected 2 days after the treatment with FFAs. Medium glucose levels were measured directly using glucose assay kit. Data were normalized to total cellular protein.

Oil red O (ORO) staining

Organoids were fixed in 4% PFA overnight at 4 °C, washed with PBS, briefly rinsed with 60% isopropanol, and stained with ORO working solution for 30 min at 37 °C in dark. Samples were rinsed once with 60% isopropanol (< 20 s), washed with PBS for 3 times, and imaged using inverted microscope (Nikon, Ti2).

Lipid droplet staining

Organoids were fixed in 4% PFA for 30 min at RT, permeabilized with 0.5% Triton X-100 for 20 min at RT, and stained with BODIPY 493/503 according to manufacturer's protocol for 20 min at RT in dark. Nuclei were counterstained with DAPI for 5 min at RT in dark. Samples were washed with PBS for 3 times between steps. Images were acquired by confocal microscopy and analyzed using ZEN 2.3 and ImageJ.

Total cholesterol (TC) measurement

Organoids were washed, resuspended in 200 μL PBS, and sonicated as described above for TG measurement. Lysates were analyzed using cholesterol assay kit (absorbance at 500 nm). Data were normalized to total protein.

Hematoxylin and eosin (H&E) staining

Organoids were fixed in 4% PFA at RT for 30 min and processed for H&E staining by Hubei Bioscience Company. Slides were scanned using digital slide scanner (TissueGnostics, strataFAXS P-S).

Reactive oxygen species (ROS) detection

ROS levels were measured in FFAs/drugs-treated organoids using commercial kit according to the manufacturer's protocol. Fluorescence intensity was quantified using microplate reader, and images were acquired by confocal microscopy.

TUNEL apoptosis assay

Teen days after the treatment with FFAs, organoids were fixed with 4% PFA for 30 min at RT, permeabilized with 0.5% Triton X-100 for 5 min at RT, and stained using TUNEL assay kit at 37 °C for 1 h in dark. Nuclei were counterstained with DAPI. Samples were washed with PBS for 3 times between steps. Images were acquired by confocal microscopy.

Western blotting

Organoids were lysed in RIPA buffer containing PMSF and protease inhibitors. Lysates were sonicated on ice (15 W power, 10 s pulse/5 sec interval, 2 cycles) and centrifuged at 14,000 rcf for 10 min at 4 °C. Supernatant protein concentration was determined by BCA assay, and each sample was subsequently diluted to same protein concentration with cell lysis buffer, then mixed with 5X loading buffer, denatured for 5 min at 100 °C, separated by SDS-PAGE with 5% stacking gel at 80 V for 20 min, then with 12% resolving gel at 120 V for 90 min, and transferred to PVDF membranes at 100 V. Membranes were blocked using 5% non-fat milk for 1 h, incubated with primary antibodies overnight. Next day, Membranes were washed and incubated with HRP-conjugated secondary antibodies for 2 h at RT, and developed using chemiluminescent substrate. Protein bands were imaged using chemiluminescence imaging system (Bio-Rad, ChemiDoc) and finally quantified using ImageJ.

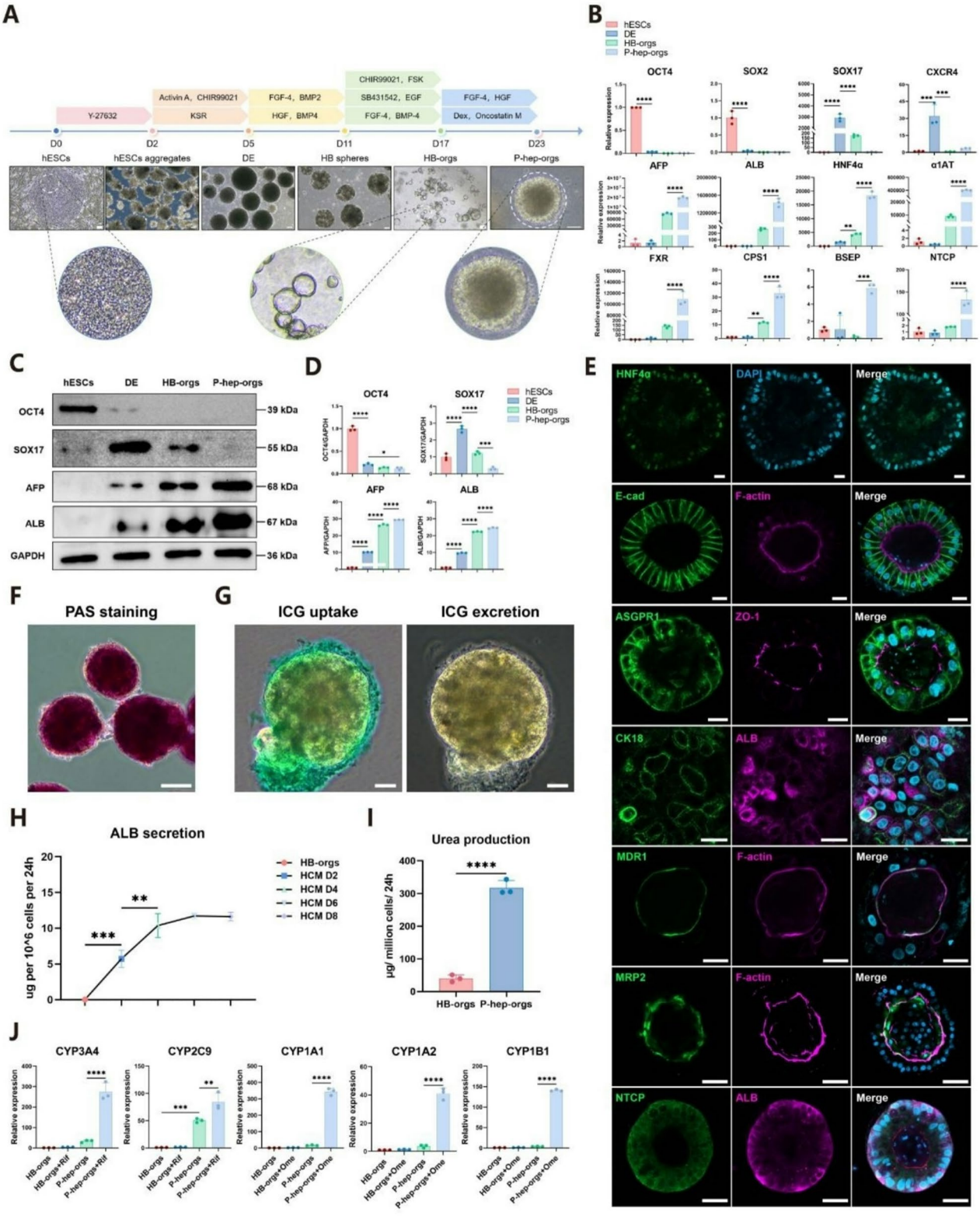


Fig. 1 (See legend on next page.)

(See figure on previous page.)

Fig. 1 Differentiation and characterization of mature polarized hepatocyte organoids from hESCs. **A** Schematic illustration of the differentiation protocol from hESCs to P-hep-orgs with representative morphological images at each stage. Scale bar = 100 μm. **B** The expression dynamics of pluripotency markers (OCT4, SOX2), definitive endoderm markers (SOX17, CXCR4), hepatocyte markers (AFP, ALB, HNF4α, α1AT, FXR, CPS1, BSEP, NTCP), were determined by qRT-PCR during the differentiation. Relative gene expression was normalized to housekeeping gene GAPDH ($n = 3$; one-way ANOVA). **C** Western blot analysis of OCT4, SOX17, AFP, ALB protein expression in hESCs, DE, HB-orgs and P-hep-orgs. Full-length blots were presented in Supplementary Fig. 1. **D** Quantified OCT4, SOX17, AFP, ALB protein levels normalized to GAPDH in (**C**) ($n = 3$; one-way ANOVA). **E** Immunofluorescence staining of P-hep-orgs for hepatocyte maturation markers (HNF4α, ASGPR1, CK18, ALB), polarization markers (ZO-1, MDR1, MRP2, NTCP), epithelial marker (E-cadherin), and cytoskeletal protein F-actin. Scale bar = 20 μm. **F** PAS staining of P-hep-orgs. Scale bar = 50 μm. **G** Evaluation of ICG uptake and excretion capacity in P-hep-orgs. Scale bar = 20 μm. **H** Secretion levels of hepatocyte functional marker ALB in culture supernatant throughout the maturation of HB-orgs to P-hep-orgs ($n = 3$; one-way ANOVA). **I** Measurement of urea production in P-hep-orgs ($n = 3$; unpaired two-tailed t-test). **J** Analysis of the inductive effects of rifampicin and omeprazole on the expression of key CYP enzymes in P-hep-orgs by RT-qPCR ($n = 3$; one-way ANOVA). Rif, Rifampicin; Ome, Omeprazole. Data were presented as mean ± SD. $^{*}P < 0.05$, $^{**}P < 0.01$, $^{***}P < 0.001$, $^{****}P < 0.0001$

RNA sequencing and analysis

Total RNAs (≥ 450 ng per sample) were sent to Novogene company for sequencing. RNA integrity was assessed using an Agilent 2100 Bioanalyzer. Libraries were prepared using NEBNext® Ultra™ RNA Library Prep Kit and sequenced on an Illumina HiSeq X-Ten platform. Raw reads were filtered to obtain clean reads, which were aligned to the human reference genome using HISAT2. Gene expression levels were quantified using FeatureCounts and FPKM (Fragments Per Kilobase of transcript per Million mapped reads). Differentially expressed genes (DEGs) were identified using DESeq2 in R (|Fold Change| ≥ 1.5, p-value ≤ 0.05). DEGs were analyzed for heatmas generation, Gene Ontology (GO) and Kyoto Encyclopedia of Genes and Genomes (KEGG) pathway enrichment using R packages and the Bioinformatics online platform (https://www.bioinformatics.com.cn).

Statistical analysis

Data are presented as mean ± standard deviation (SD). Statistical significance was assessed using multiple Student's t-tests, one-way ANOVA or two-way ANOVA in GraphPad Prism 9.0.0. p-value < 0.05 was considered statistically significant.

Results

Differentiation and characterization of mature polarized hepatocyte organoids derived from hESCs

To obtain P-hep-orgs suitable for the development of MASLD model, we employed an established laboratory differentiation protocol described previously [24]. H9 cells (a hESCs line) were sequentially differentiated into definitive endoderm (DE), hepatoblast spheres (HB spheres), hepatoblast organoids (HB-orgs), and finally P-hep-orgs under specific conditions (Fig. 1A). Morphological observations revealed that hESCs exhibited typical clonal growth with small, round cells and minimal intercellular gaps. Upon the differentiation to DE stage, 3D suspension-cultured spheroids displayed smooth edges. Upon reaching HB sphere stage, the spheroids developed rougher edges and internal vacuoles. At HB-orgs stage, hepatoblasts formed a monolayer within a growth factor-reduced (GFR) Matrigel matrix and exhibited a vacuolated morphology. These HB-orgs were then matured for 6 days in HCM medium supplemented with GFR Matrigel, yielding P-hep-orgs, which comprised a monolayer of columnar polarized hepatocytes.

To validate the differentiation trajectory, RT-qPCR analysis of stage-specific markers was performed. As shown in Fig. 1B–D, the expression of pluripotency markers OCT4 and SOX2 was significantly downregulated during the differentiation. Endoderm markers SOX17 and CXCR4 were expressed at low levels in hESCs, increased sharply upon the differentiation into DE stage, and then declined significantly. The expression levels of hepatocyte mature markers (ALB, HNF4α, α1AT, FXR, CPS1) and polarization markers (BSEP, NTCP) were increased significantly with differentiation progression, consistent with gene expression trends during in vivo hepatocyte maturation. Immunofluorescence staining demonstrated that day-6 P-hep-orgs expressed key mature hepatocyte (HNF4α, ASGPR1, CK18, ALB) and epithelial (E-cad) markers (Fig. 1E). Furthermore, these organoids exhibited a hollow, monolayered columnar architecture with established structural polarity. This polarity was demonstrated by the specific localization of apical markers (ZO-1, MDR1, MRP2) to the luminal membrane and the basolateral marker NTCP to the non-luminal domain (Fig. 1E). Functional characterization demonstrated that P-hep-orgs possess key hepatic functions, including glycogen storage (Fig. 1F), ICG uptake and excretion (Fig. 1G), albumin (ALB) synthesis and secretion (Fig. 1H), urea production (Fig. 1I), and inducible expression of key cytochrome P450 (CYP450) enzymes (Fig. 1J). Collectively, our data demonstrate the generation of mature, polarized hepatocyte organoids with key functional hepatic capacities.

Development and characterization of P-hep-org-based MASLD model with Glucose-Lipid metabolic dysregulation

Building on mature hepatocyte functionality and polarized structure of P-hep-orgs, we established MASLD model using these organoids. Adopting a widely utilized modeling approach, a free fatty acid (FFA) mixture (oleic

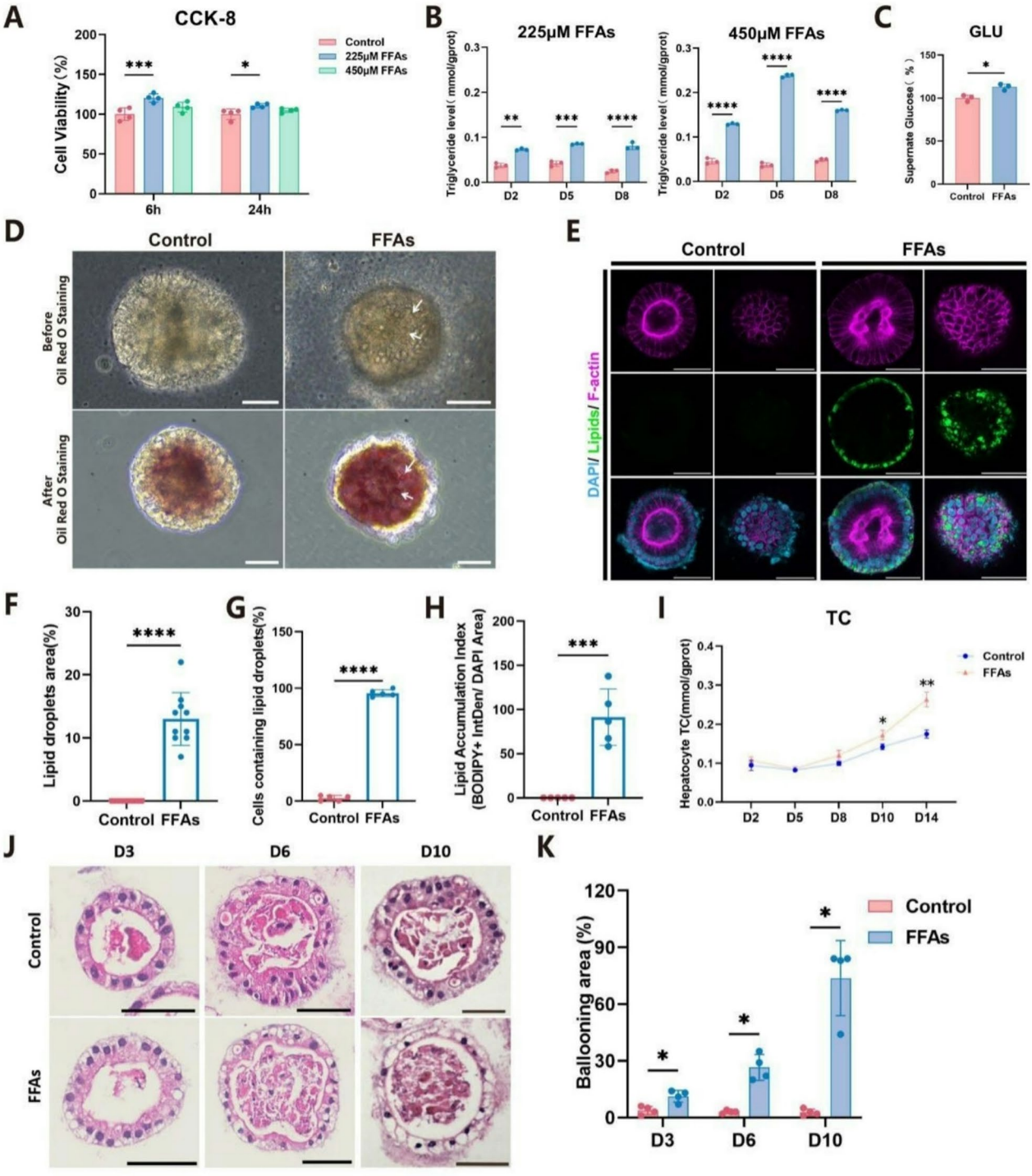


Fig. 2 Development and characterization of P-hep-org-based model of MASLD with glucose-lipid metabolic dysregulation. **A** Cytotoxicity assays of FFAs on P-hep-orgs ($n=4$; one-way ANOVA). **B** Comparison of triglyceride (TG) accumulation in P-hep-orgs produced by the treatment with FFAs at different concentrations ($n=3$; two-way ANOVA). **C** Glucose secretion levels in culture supernatant following the treatment with FFAs ($n=3$; unpaired two-tailed t-test). **D** Oil Red O staining showing lipid droplet accumulation in P-hep-orgs treated with FFAs. Granular deposits indicated by white arrows, scale bar = 50 μm. **E** BODIPY staining of lipid droplets (green) in P-hep-orgs treated with FFAs, scale bar = 50 μm. **F**, **G**, **H** Quantitative analysis of (**F**) BODIPY-positive area ($n=10$), **G** proportion of lipid droplet-containing hepatocytes ($n=5$) and (H) BODIPY fluorescence intensity ($n=5$) in P-hep-orgs; unpaired two-tailed t-test. **I** Cholesterol content dynamics in P-hep-orgs during prolonged treatment with FFAs ($n=3$; two-way ANOVA). **J** Hematoxylin and eosin (H&E) staining revealing hepatocyte ballooning degeneration. Scale bar = 50 μm. **K** Quantification of ballooning degeneration area in (**J**) ($n=4$; two-way ANOVA). Data were presented as mean ± SD. *$P<0.05$, **$P<0.01$, ***$P<0.001$, ****$P<0.0001$

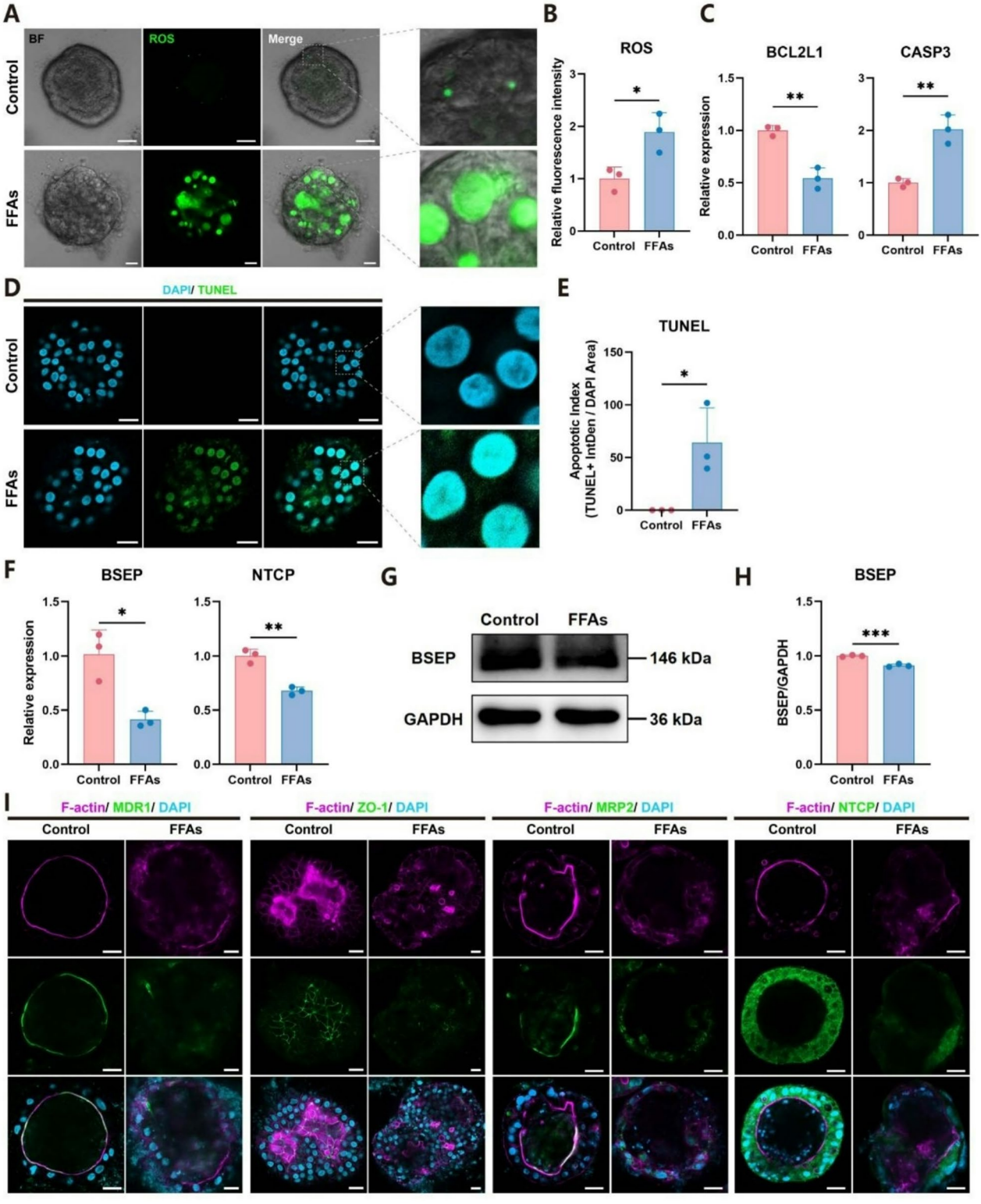


Fig. 3 (See legend on next page.)

(See figure on previous page.)

Fig. 3 Characterization of hepatocyte injury and structural disruption in P-hep-org-based model of MASLD. **A** Fluorescence detection of ROS levels in P-hep-orgs treated with FFAs for 2 days. BF, bright field. Scale bar = 20 μm. **B** Quantification of ROS fluorescence intensity in P-hep-orgs using microplate reader ($n = 3$; unpaired two-tailed t-test). **C** The relative expression levels of apoptosis regulators BCL2L1 (anti-apoptotic) and CASP3 (pro-apoptotic) were determined by qRT-PCR in P-hep-orgs 24 h after the exposure to FAAs ($n = 3$; unpaired two-tailed t-test). **D** TUNEL assay detecting apoptotic cells in P-hep-orgs 10 days after the treatment with FFAs. Scale bar = 20 μm. **E** Quantitative analysis of TUNEL fluorescence intensity ($n = 3$; unpaired two-tailed t-test). **F** The relative expression levels of polarization markers BSEP and NTCP in P-hep-orgs were determined by qRT-PCR 10 days post the treatment with FFAs ($n = 3$; unpaired two-tailed t-test). **G** Western blot analysis of BSEP protein expression in P-hep-orgs treated with FFAs for 10 days. Full-length blots were presented in Supplementary Fig. 2. **H** Quantified BSEP protein levels normalized to GAPDH in (**G**) ($n = 3$; unpaired two-tailed t-test). **I** Protein localization detection of polarization markers (MDR1, ZO-1, MRP2, NTCP) and cytoskeleton marker (F-actin) by immunofluorescence staining in P-hep-orgs 10 days post the treatment with FFAs. Scale bar = 20 μm. Data were presented as mean ± SD. $^{*}P < 0.05$, $^{**}P < 0.01$, $^{***}P < 0.001$

acid OA/palmitic acid PA = 2:1) simulated diet-induced lipid accumulation to identify optimal modeling concentrations. CCK-8 cytotoxicity assays demonstrated that neither 225 μM FFAs (150 μM OA + 75 μM PA) nor 450 μM FFAs (300 μM OA + 150 μM PA) significantly reduced the viability of P-hep-orgs after short-term exposure (6–24 h) (Fig. 2A), notably, 225 μM FFAs transiently enhanced the viability. Triglyceride (TG) quantification revealed significantly elevated intracellular TG levels in P-hep-orgs at day 2 after the treatments of both concentrations with 450 μM FFAs to induce a stronger effect than 225 μM FFAs did (Fig. 2B), leading to the selection of 450 μM FFAs for subsequent modeling. Under MASLD conditions, the lipotoxicity activates the gluconeogenesis, thereby increasing blood glucose levels. Treatment with 450 μM FFAs for 2 days resulted in a significant 14% rise in supernatant glucose levels (Fig. 2C), indicating disrupted glucose metabolism in the model. Oil Red O staining and light microscopy revealed granular red lipid droplet deposition specifically in FFAs-treated P-hep-orgs (Fig. 2D). The accumulation of lipid droplets within P-hep-orgs was visualized by combined BODIPY and phalloidin staining two days after FFA exposure (Fig. 2E–H). Quantitative analysis indicated that lipid droplet area coverage was approximately 13% (Fig. 2F), with lipid accumulation detected in over 90% of hepatocytes (Fig. 2G). Furthermore, total cholesterol (TC) contents in P-hep-orgs were significantly increased by day 10 of FFAs treatment (Fig. 2I). Hematoxylin and eosin (H&E) staining revealed progressive ballooning degeneration in P-hep-orgs with prolonged FFA exposure (Fig. 2J and K), consistent with MASLD pathological progression. Collectively, these results provide evidence for the establishment of a P-hep-org-based MASLD model and systematically characterize its associated glucose-lipid metabolic dysregulation and hallmark pathological phenotypes.

Characterization of hepatocyte injury and structural disruption in MASLD model

Oxidative stress, a key pathological process in MASLD progression, involves the accumulation of excessive reactive oxygen species (ROS) due to mitochondrial electron transport chain (ETC) overload from β-oxidation of surplus FFAs. This overload causes electron accumulation at ETC intermediates (e.g., coenzyme Q), which react with O_2 to generate superoxide anion (O_2^-). Here, 450 μM FFAs treatment for 2 days significantly increased intracellular ROS levels in P-hep-orgs (Fig. 3A and B). During the development of MASLD, FFAs synergistically induce hepatocyte apoptosis through various pathways, including oxidative stress and the accumulation of lipotoxic metabolites. RT-qPCR analysis revealed that 24-hour FFA treatment suppressed anti-apoptotic gene *BCL2L1* and enhanced pro-apoptotic gene *CASP3* (Fig. 3C). TUNEL assays further revealed FFAs-induced apoptosis in P-hep-orgs after 10-day FFAs exposure, evidenced by nuclear-localized green fluorescence signals (Fig. 3D and E). Previous studies have demonstrated that polarized structure of hepatocytes becomes disrupted during the progression of MASLD [14, 20, 25]. We also found that 10-day FFAs treatment significantly reduced the expression of apical membrane marker BSEP both transcriptionally and translationally, and suppressed basolateral marker NTCP transcriptionally in P-hep-orgs through RT-qPCR and Western blot analyses (Fig. 3F–H). Moreover, immunofluorescent staining further revealed the mis-localization of cytoskeletal protein F-actin, apical transporter (MDR1, MRP2), basolateral transporter NTCP and tight junction protein ZO-1 (Fig. 3I). Collectively, the treatment with FFAs recapitulated core pathological phenotypes of MASLD, including hepatocyte injury and structural disorganization in P-hep-orgs.

Transcriptomic alterations in P-hep-org-Based MASLD model during disease progression

To investigate transcriptomic alterations induced by FFAs, RNA sequencing of P-hep-orgs treated for 2 or 10 days with matched controls was performed. We identified 630 and 2,738 differentially expressed genes (DEGs; $|FC| \geq 1.5$, $P \leq 0.05$) at respective timepoints, demonstrating progressive exacerbation of FFAs-induced transcriptomic alterations over time (Fig. 4A and B). GO enrichment analysis revealed that upregulated DEGs were associated with key MASLD-relevant processes, including fatty acid metabolism, glucose metabolism, insulin response, inflammation, and apoptosis regulation (Fig. 4C). Conversely, downregulated DEGs participated

in processes such as extracellular matrix organization, tissue homeostasis, calcium transport, tissue remodeling, and steroid hormone response. Besides, GO enrichment analysis revealed that early-stage phenotypes (e.g., lipid accumulation, fatty acid oxidation) were significantly upregulated at both time points, with effects intensifying after 10 days of FFAs treatment (Fig. 4D). However, advanced-stage phenotypes (e.g., apoptosis, inflammation) were markedly expressed by day 10 (Fig. 4E). These results revealed the temporal escalation of cell fate-altering processes throughout disease progression. KEGG analysis demonstrated enrichment of both DEG sets in core MASLD progression pathways, including PPAR signaling for glucose/lipid metabolic regulation, MAPK signaling for the apoptosis, TGF-β fibrogenic signaling (Fig. 4F and G), encompassing the essential signaling network underlying the pathogenesis of MASLD. In conclusion, the treatment of models with FFAs for 2 days recapitulated early pathology of MASL (e.g., lipid accumulation, fatty acid oxidation), whereas the treatment model for 10 days mimicked advanced phenotypes of MASH (e.g., apoptosis, inflammation).

Dysfunction and ductular reaction in P-hep-org-based MASLD model

Transcriptomic analysis revealed FFAs-induced progressive hepatic dysfunction in P-hep-orgs, characterized by significant downregulation of hepatocyte functional and metabolic markers that intensified with prolonged treatment (Fig. 5A). Experimental validation demonstrated that the exposure to FFAs for 10 days substantially suppressed both mRNA expression and secreted protein levels of core hepatocyte function marker ALB (Fig. 5B and C). Functional assays demonstrated that FFAs impaired urea production (Fig. 5D) and reduced drug metabolism capacity (Fig. 5E) of P-hep-orgs. Concurrently, heatmaps of DEGs indicated FFAs-mediated upregulation of ductular reaction (DR) markers (Fig. 5A), with RT-qPCR showing elevated the expression of cholangiocyte markers (CK7, HES1, AE2, MRP3) (Fig. 5F). Western blot further validated increased CK7 protein expression (Fig. 5G and H). DR, an adaptive repair mechanism to chronic liver injury, features reactive biliary proliferation and periductal fibrosis. FFAs-triggered upregulation of DR markers in this model indicated P-hep-orgs recapitulated ductular reaction under injury conditions.

Transcriptomic concordance between human MASH livers and P-hep-org-based MASLD model

We assessed the transcriptional similarity between our FFA-induced P-hep-org model and human MASLD by comparing its transcriptomic data with GEO dataset GSE126848 (MASH patients vs. Healthy individuals). The analysis of overlapping gene sets revealed 581 genes shared between two datasets (Fig. 6A). Heatmap analysis demonstrated a significant similarity in dysregulated gene expression between human MASH livers and 10-day FFA-treated P-hep-orgs (Fig. 6B). This shared signature encompassed key gene sets of metabolic dysfunction—including lipid and glucose metabolism, insulin resistance, and ER/oxidative stress as well as cell fate regulation processes such as apoptosis, senescence, and inflammation. Venn analysis demonstrated a substantial overlap in enriched KEGG pathways between our model and human MASH (Fig. 6C). These co-enriched pathways included core signaling networks critical to MASLD progression, such as PI3K-Akt, PPAR, MAPK, TNF, NF-κB, and TGF-β (Fig. 6D and E). These findings provide evidence that 10-day FFA-treated P-hep-orgs partially recapitulate molecular features of human MASH livers at the transcriptomic level (Fig. 6A–E).

Evaluation of applicability for drug screening using P-hep-org-based MASLD model

Studies have reported that the antioxidant or lipid-lowering agent vitamin E (VE), ursodeoxycholic acid (UDCA), and empagliflozin (EMPA) can ameliorate MASLD phenotypes [26–28]. Referencing reported concentrations (100 μM VE, 200 μM UDCA, 10 μM EMPA), we tested the cell viability with drug concentration gradients [26–28]. We used CCK-8 assay to assess cytotoxicity and select appropriate drug concentrations. The results (Fig. 7A) showed that VE (0–500 μM) did not impair cell viability, strikingly, 100 μM VE significantly enhanced it. UDCA was non-toxic at 0–200 μM but toxic at 500 μM, while EMPA was safe at 0–10 μM but cytotoxic at ≥ 20 μM. Based on these results, we selected 100 μM VE, 200 μM UDCA, and 10 μM EMPA for all subsequent experiments.

Following the treatment of 450 μM FFAs-induced model for 2 days, all three drugs significantly reduced lipid droplet accumulations (Fig. 7B and C) and lowered triglyceride contents (Fig. 7D). Ten days after FFA exposure, we administered a 4-day drug treatment. Cholesterol assays revealed that both 100 μM VE and 200 μM UDCA attenuated cholesterol accumulation, whereas 10 μM EMPA lacked this effect (Fig. 7E). RT-qPCR analysis demonstrated that all three drugs upregulated genes involved in fatty acid oxidation (e.g., ACADVL, ACADM) and lipid efflux (ABCA1, ABCG1) (Fig. 7F), indicating their potential mechanism of action involves enhancing lipid metabolism and export. Regarding FFA-induced oxidative stress, fluorescence detection and microplate quantification demonstrated that VE and EMPA significantly suppressed elevated ROS levels (Fig. 7G and H), whereas UDCA showed no such activity. Furthermore, liver function restoration assays indicated that UDCA and EMPA upregulated both mRNA expression (Fig. 7I)

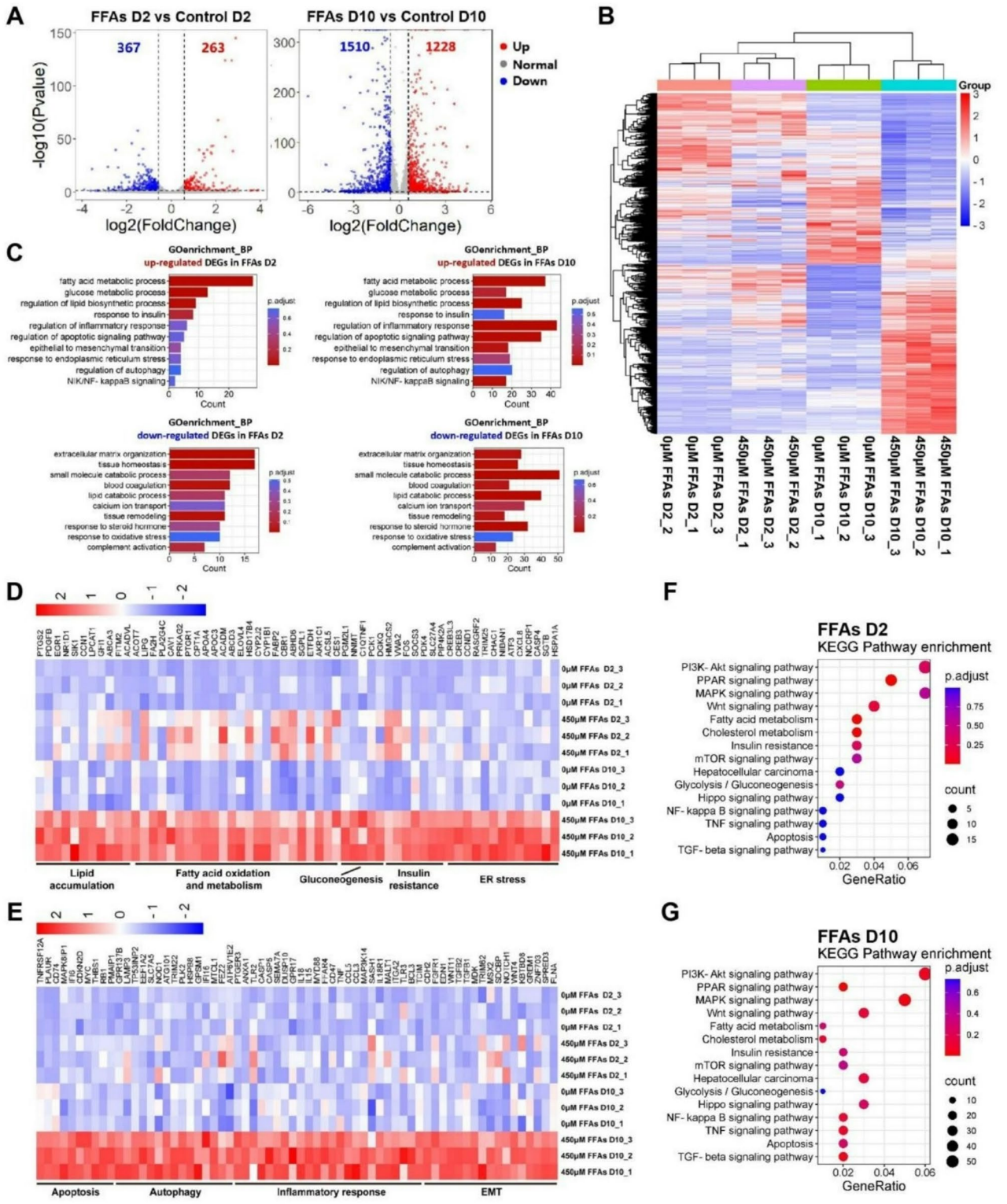


Fig. 4 Transcriptomic alterations in P-hep-org-based model of MASLD during disease progression. **A** Volcano plots of differentially expressed genes (DEGs) in P-hep-orgs with or without the treatment with FFAs for 2 days (left) and 10 days (right). **B** Heatmap of DEGs in P-hep-orgs with different treatments. **C** Gene Ontology (GO) biological process enrichment for DEGs. **D**, **E** Heatmaps of early-stage (**D**, the treatment with FFAs for 2 days) and advanced-stage (**E**, the treatment with FFAs for 10 days) MASLD phenotype-related DEGs. **F** KEGG pathway enrichment analysis of DEGs following a 2-day FFA treatment. Among MASLD-relevant pathways analyzed, PPAR signaling pathway, fatty acid metabolism, and cholesterol metabolism met the significance threshold (p.adjust < 0.05). **G** KEGG pathway enrichment analysis of DEGs following a 10-day FFA treatment. Among MASLD-relevant pathways analyzed, PPAR signaling pathway, MAPK signaling pathway, and TGF-beta signaling pathway met the significance threshold (p.adjust < 0.05)

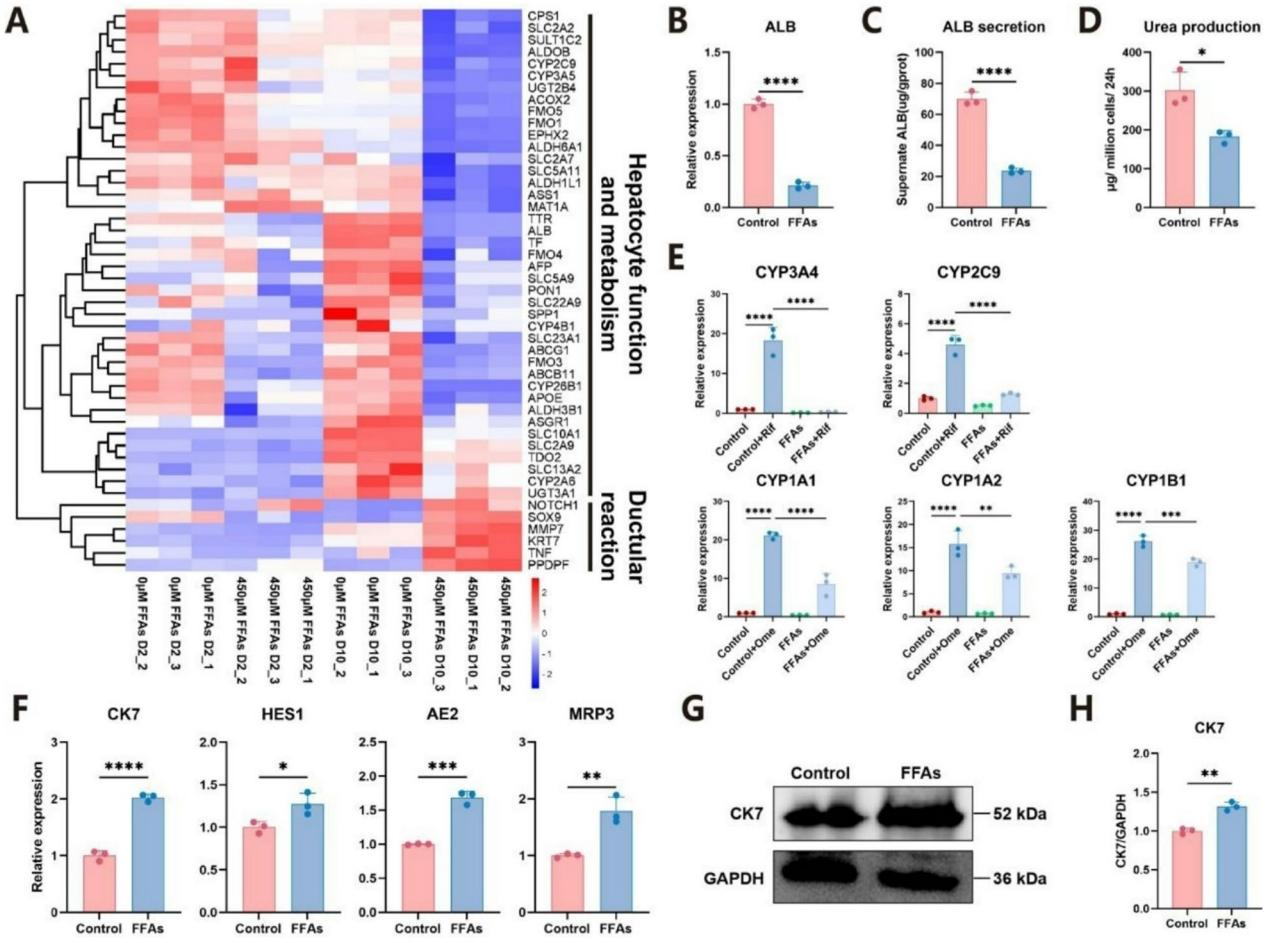


Fig. 5 Hepatic dysfunction and ductular reaction in P-hep-orgs- MASLD model of MASLD. **A** Heatmap of hepatic function, metabolism, and ductular reaction markers in P-hep-orgs with or without FFA-treatment. **B** The relative expression of albumin (ALB) in P-hep-orgs with or without FFA-treatment for 10 days ($n=3$; unpaired two-tailed t-test). **C** ALB secretion dynamics in culture supernatant of P-hep-orgs 10 days after FFA-treatment ($n=3$; unpaired two-tailed t-test). **D** Measurement of urea production in P-hep-orgs with or without FFA-treatment ($n=3$; unpaired two-tailed t-test). **E** Analysis of the inductive effects of rifampicin and omeprazole on the expression of key CYP enzymes in P-hep-orgs with or without FFA-treatment by RT-qPCR ($n=3$; one-way ANOVA). **F** The relative expression levels of cholangiocyte markers were determined by qRT-PCR in P-hep-orgs following the exposure to FFAs for 10 days ($n=3$; unpaired two-tailed t-test). **G** Western blot of cholangiocyte marker CK7 protein in P-hep-orgs 10 days after the treatment with FFAs. Full-length blots were presented in Supplementary Fig. 3. **H** Quantified CK7 protein levels normalized to GAPDH in (**G**) ($n=3$; unpaired two-tailed t-test). Data were presented as mean ± SD. *$P<0.05$, **$P<0.01$, ***$P<0.001$, ****$P<0.0001$

and protein secretion (Fig. 7J) of ALB, VE exhibited no effect on the expression of ALB. In summary, this model provided experimental evidence supporting the efficacy of three antioxidant or lipid-lowering drugs against key MASLD pathological phenotypes, suggesting its potential for screening novel MASLD therapeutics.

Discussion

There remains an urgent need for disease models that faithfully recapitulate the progression of MASLD to facilitate mechanistic studies and therapeutic discovery. Current animal models of MASLD are constrained by prolonged induction times, significant batch-to-batch variability, and inherent species differences [7–9]. While cell models of MASLD circumvent some limitations of animal studies, however, they often inadequately replicate the structural and functional complexity of human hepatocytes in vivo. To address these critical gaps, we generated P-hep-orgs from hESCs and then established MASLD model by inducing them with FFAs. This model addresses some key limitations of existing systems. Compared with mouse model established by ZHOU Y, et al. [29], the organoid model developed in this study offers human-relevant advantages (Fig. 1A) and requires a considerably shorter modeling period—completing both disease induction and drug screening within only two weeks (Fig. 7B–E and G–J). Compared with cell-based model constructed by WANG L, et al. [30], our study provides more comprehensive validation of hepatocyte organoids, including assessments of hepatic functions

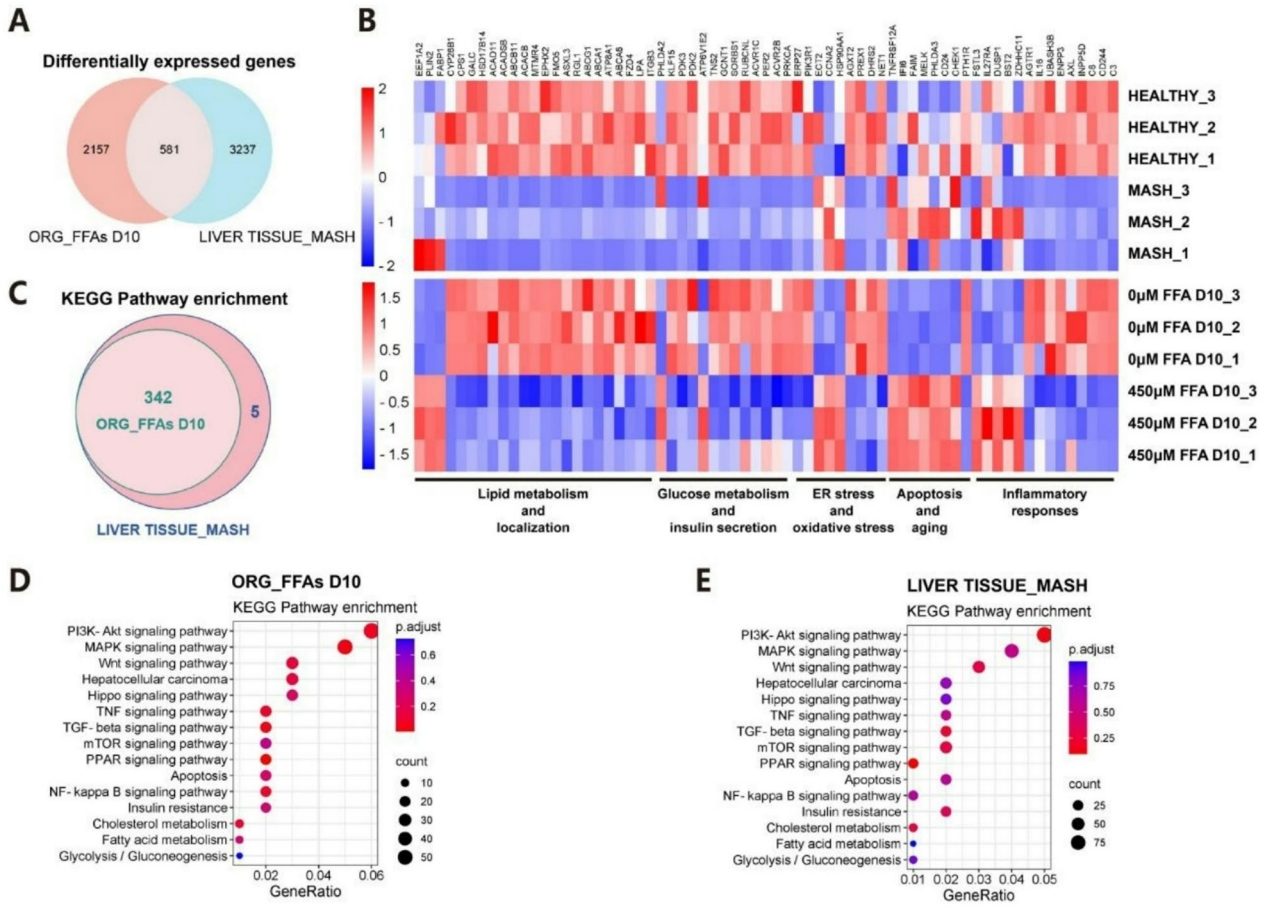


Fig. 6 Transcriptomic congruence between human livers of MASH and P-hep-org-based model of MASLD. **A** Overlap DEGs analysis between 10-day FFAs-treated P-hep-orgs and human MASH liver specimens. **B** Heatmap of metabolic dysfunction-associated DEGs in human MASH liver specimens (top) vs. FFAs-treated P-hep-orgs for 10 days (bottom). The samples HEALTHY_1, HEALTHY_2, HEALTHY_3, MASH_1, MASH_2, and MASH_3 correspond respectively to patient data X0869 X0877 X0887 X3997 X4000 and X4008 contained within GSE126848 dataset. **C** Overlap of significantly enriched KEGG pathways in DEG sets from MASH livers and MASLD model. **D**, **E** KEGG pathways linked to MASLD progression enriched in MASLD model (**D**) and human MASH livers (**E**)

such as glycogen storage (Fig. 1F) and urea production (Fig. 1I), as well as expression of polarization markers like MRP2 (Fig. 1E), thereby more thoroughly demonstrating structural and functional maturation. Single-cell transcriptomic analysis revealed that the differentiated HB-orgs resemble human fetal liver at gestational week 6 [24, 31, 32], and importantly, 43% of hepatocytes within P-hep-orgs demonstrated functional maturity comparable to PHHs [24, 33]. Relative to primary hepatocyte-derived organoid model developed by HU H, et al. [34], our hESC-based system presents distinct advantages in terms of the scalability and reproducibility. While primary hepatocyte-derived organoids are constrained by donor scarcity and inherent batch-to-batch heterogeneity, our approach provides a renewable and consistent cell source. This enhances the utility of the model for large-scale, standardized applications in pharmaceutical screening and fundamental mechanistic studies.

Critically, FFAs induction recapitulated the temporal progression of key pathological phenotypes of MASLD. The model sequentially exhibited early-stage glucolipid metabolic dysregulation (Fig. 2B–K) and oxidative stress (Fig. 3A and B), progressing to advanced-stage features including hepatocyte apoptosis (Fig. 3C–E), liver dysfunction (Fig. 5A–E), and ductular reaction (Fig. 5A and F–H). Transcriptomic analysis further validated the pathological relevance of the model. The treatment with FFAs for 10 days induced 2738 DEGs significantly enriched in pathways associated with lipotoxic stress, inflammatory activation, and cell fate regulation (Fig. 4C–G). This molecular signature exhibited substantial overlap with hepatic transcriptome profiles of patients with MASH (Fig. 6A–E). The observed time-dependent gene expression patterns, such as early upregulation of gluconeogenesis genes followed by later activation of the apoptosis and epithelial-mesenchymal transition (EMT) pathways, closely mirrored progression dynamics of MASLD.

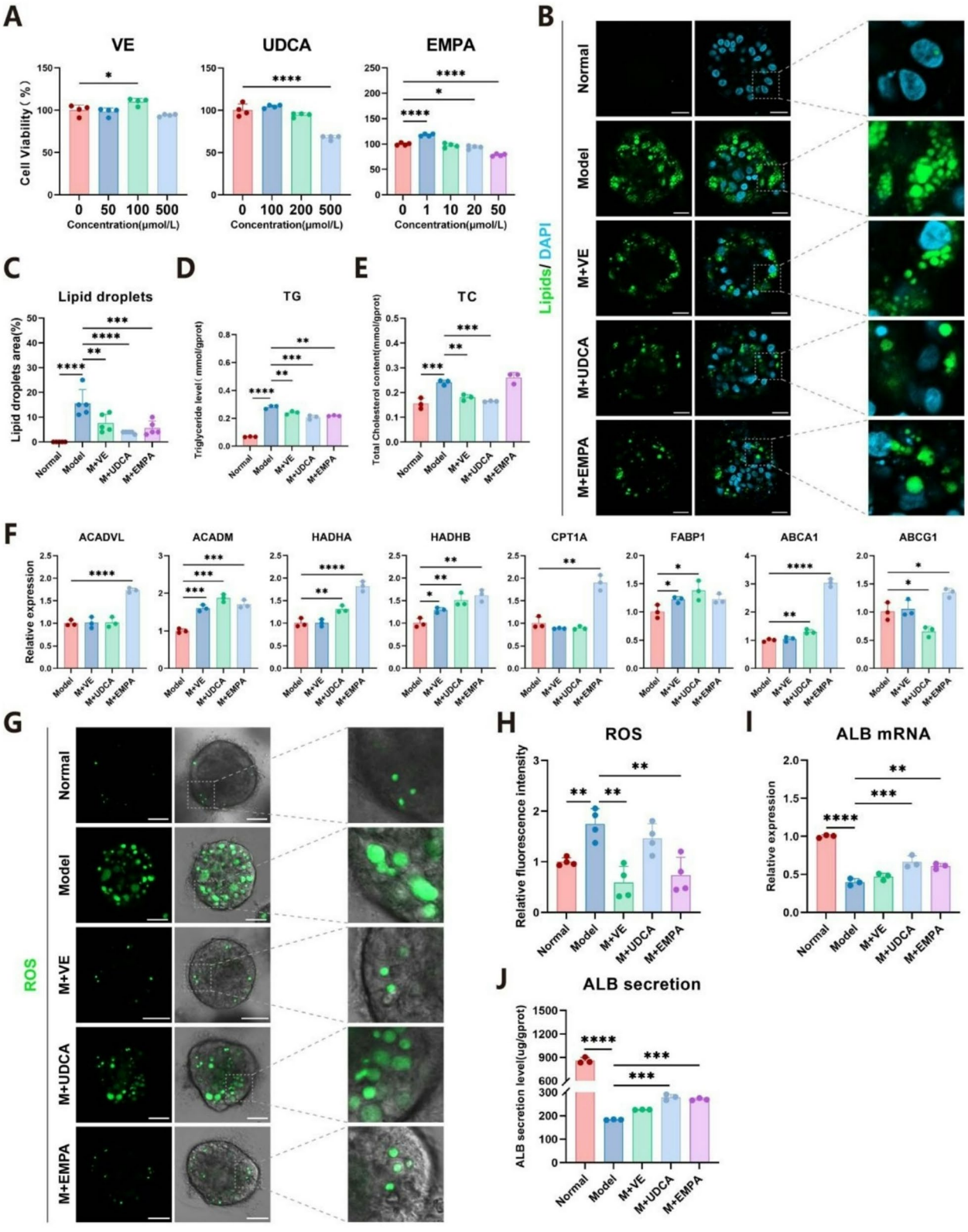


Fig. 7 (See legend on next page.)

(See figure on previous page.)

Fig. 7 Evaluation of the applicability for drug screening using P-hep-org-based model of MASLD. **A** Cytotoxicity assessment of antioxidative or lipid-lowering drugs via CCK-8 assay ($n=4$; one-way ANOVA). VE, vitamin E; UDCA, ursodeoxycholic acid; EMPA, empagliflozin. **B** BODIPY staining showing drug effects on FFAs-induced lipid droplets. Scale bar = 20 μm. **C** Quantified BODIPY fluorescence intensity from (**B**) ($n=5$; one-way ANOVA). **D**, **E** Drug-mediated reduction of FFAs-induced triglyceride (**D**) and cholesterol (**E**) accumulation ($n=3$; one-way ANOVA). **F** Expression modulation of fatty acid oxidation genes (ACADVL, ACADM, HADHA, HADHB, CPT1A, FABP1) and lipid efflux genes (ABCA1, ABCG1) by drugs ($n=3$; one-way ANOVA). **G** Detection of intracellular ROS levels after drug treatment. Scale bar = 20 μm. **H** Quantification of ROS fluorescence intensity from (**G**) ($n=3$; one-way ANOVA). **I**, **J** RT-qPCR (**I**) and ELISA (**J**) validation of ALB expression recovery by drugs ($n=3$; one-way ANOVA). Data were presented as mean ± SD. $^{*}P<0.05$, $^{**}P<0.01$, $^{***}P<0.001$, $^{****}P<0.0001$

Furthermore, this model captured hallmark pathological features which was often elusive in previous models [30, 35], including hepatocyte ballooning degeneration (Fig. 2J and K) and progressive disruption of the polarization (Fig. 3F–I). These observations provide novel insights into the mechanisms of hepatocyte depolarization during the pathogenesis of MASLD. This spectrum of phenotypic changes provides a useful platform for investigating the mechanisms of MASLD progression. The utility of this model for therapeutic screening was demonstrated. We validated the efficacy of three clinical agents Vitamin E (VE), Ursodeoxycholic Acid (UDCA), and Empagliflozin (EMPA) in ameliorating key phenotypes of MASLD within the model. All three compounds significantly reduced lipid accumulation (Fig. 7B–E). VE and EMPA effectively suppressed ROS accumulation (Fig. 7G and H). Notably, UDCA and EMPA demonstrated previously unreported ability to restore Albumin (ALB) expression (Fig. 7I and J), suggesting a potential benefit on hepatocyte synthetic function. This heterogeneity in therapeutic response not only aligns with established drug properties [26–28], but also underscores the model's sensitivity in distinguishing distinct mechanisms of the action, supporting its potential utility in MASLD drug discovery.

Interestingly, we observed that 225 μM FFAs transiently enhanced the viability of P-hep-orgs (Fig. 2A), a phenomenon not previously reported. This might be explained by potential stimulatory effects of low-concentration FFAs. One possibility is that low-level FFAs acts as a mild stressor [36], temporarily activating adaptive protection mechanisms such as mild mitochondrial uncoupling to reduce ROS production, thereby boosting energy metabolism. Alternatively, FFAs might be utilized as an efficient substrate [37] via β-oxidation, temporarily increasing ATP production before the lipotoxicity occurs at higher doses. This viability-promoting effect merits further investigation. Besides, the observed FFA-induced ductular reaction (Fig. 5), along with transcriptomic evidence of inflammatory pathway activation (Fig. 4E and G) and oxidative stress (Fig. 3A and B), suggests a potential link to microenvironmental stress in our model. However, as the system lacks non-parenchymal cells such as Kupffer cells, key producers of cytokines like TNF-α and IL-6, the inflammatory signals likely reflect hepatocyte-driven responses rather than immune-mediated inflammation. While this limits mechanistic interpretation, our findings lay groundwork for future studies using multicellular co-culture systems to explore ductular reaction in the context of organized inflammation and oxidative stress.

In conclusion, we have developed and validated a novel in vitro model of MASLD using mature polarized hepatocyte organoids derived from hESCs. This model recapitulated the sequential pathological transitions from the steatosis and oxidative stress to the inflammation and functional impairment observed in the progression of human MASLD. Its physiological relevance was systematically illustrated through structural, functional, and transcriptomic analyses. Furthermore, the model demonstrated high efficiency and reliability in preclinical drug screening, effectively distinguishing therapeutic profiles of known clinical agents. This platform offers a more efficient, scalable, and biologically faithful tool for investigating the pathogenesis of MASLD and accelerating the discovery of novel therapeutics, with the identified candidates serving as prime targets for subsequent validation in animal models.

Abbreviations

MASLD	Metabolic dysfunction-associated steatotic liver disease
hESCs	Human embryonic stem cells
P-hep-orgs	Polarized hepatocyte organoids
FFAs	Free fatty acids
MASH	Metabolic dysfunction-associated steatohepatitis
NAFLD	Non-alcoholic fatty liver disease
2D	Two-dimension
hPSCs	Human pluripotent stem cells
3D	Three-dimension
HB-orgs	Hepatoblast organoids
HB	Hepatoblast
MTAs	Material Transfer Agreements
KSR	Knockout Serum Replacement
DE	Definitive endoderm
GCDR	Gentle Cell Dissociation Reagent
PSA	Penicillin-Streptomycin-Amphotericin B
GFR	Growth Factor Reduced
ECM	Extracellular matrix
HCM	Hepatocyte Culture Medium
RT-qPCR	Reverse transcription quantitative polymerase chain reaction
GAPDH	Glyceraldehyde-3-phosphate dehydrogenase
IF	Immunofluorescence
PFA	Paraformaldehyde
RT	Room temperature
PBS	Phosphate-buffered saline
ALB	Albumin
PAS	Periodic Acid-Schiff
ICG	Indocyanine green
Rif	Rifampicin
Ome	Omeprazole

OA	Oleic acid
PA	Palmitic acid
CCK-8	Cell Counting Kit-8
TG	Triglyceride
ORO	Oil Red O
TC	Total cholesterol
H&E	Hematoxylin and eosin
ROS	Reactive oxygen species
DEGs	Differentially expressed genes
GO	Gene Ontology
KEGG	Kyoto Encyclopedia of Genes and Genomes
SD	Standard deviation
ETC	Electron transport chain
ER	Endoplasmic reticulum
EMT	Epithelial-mesenchymal transition
DR	Ductular reaction
VE	Vitamin E
UDCA	Ursodeoxycholic acid
EMPA	Empagliflozin
HPHs	Human Primary Hepatocytes
NPCs	Non-parenchymal cells

Supplementary Information

The online version contains supplementary material available at https://doi.org/10.1186/s13287-025-04865-7.

Supplementary material 1.

Acknowledgements
Not applicable.

Author contributions
Y.Y.D., C.L.Q., H.B.W. and Y.J.Z. conceived and designed the experiments. C.L.Q performed the experiments, collected and analyzed data. C.L.Q. and P.L.L. prepared the manuscript. H.B.W. and J.H.X. involved in bioinformatics analysis. P.L.L., W.J.Y., X.Y.S., S.P.L., S.C., X.T.C. contributed to the collection of the data. Y.Y.D. and Y.J.Z. provided financial support.

Funding
This work was funded in part by National Key Research and Development Program of China (2018YFA0108201), by Research Starting Funding of South China University of Technology (D6201880, K5180910, K5204120, and D6212440), by Research Starting Funding of the Second Affiliated Hospital of South China University of Technology (KY09060026), by Research Agreement between South China University of Technology and Guangzhou First People's Hospital (D9194290), by Foundation of Guangzhou Key Clinical Specialties (Institute of Clinical Medicine) (2024–2026), by Project of Key Medical Discipline in Guangzhou (2025–2027).

Data availability
The data and materials that support the findings of this study are available from the corresponding author upon reasonable request. Original data of RNA-seq has been deposited in GEO with accession number GSE303090.

Declarations

Ethics approval and consent to participate
Not applicable.

Consent for publication
The authors have given the consent for publication.

Competing interests
The authors declare no competing interests.

Author details
[1]Department of Gastroenterology and Hepatology, Guangzhou Digestive Disease Center, the Second Affiliated Hospital, School of Medicine, South China University of Technology, Guangzhou 510180, China
[2]Laboratory of Stem Cells and Translational Medicine, Center for Medical Research on Innovation and Translation, Institute of Clinical Medicine, Second Affiliated Hospital, School of Medicine, South China University of Technology, Guangzhou 510180, China
[3]Laboratory of Stem Cells and Translational Medicine, Institute for Life Science, School of Medicine, South China University of Technology, Guangzhou 510006, China
[4]School of Life Sciences, Zhaoqing University, Zhaoqing 526061, China
[5]National Engineering Research Center for Tissue Restoration and Reconstruction, South China University of Technology, Guangzhou 510006, China
[6]The Innovation Centre of Ministry of Education for Development and Diseases, the Second Affiliated Hospital, School of Medicine, South China University of Technology, Guangzhou 510006, China
[7]Laboratory of Stem Cells and Translational Medicine, Institute for Clinical Medicine, The Second Affiliation Hospital, School of Medicine, South China University of Technology, No.1 Panfu Road, Guangzhou 510180, China
[8]Department of Gastroenterology and Hepatology, Guangzhou Digestive Disease Center, The Second Affiliation Hospital, School of Medicine, South China University of Technology, No.1 Panfu Road, Guangzhou 510180, China

Received: 20 August 2025 / Accepted: 10 December 2025
Published online: 20 December 2025

References

1. Israelsen M, Francque S, Tsochatzis EA, et al. Steatotic liver disease. Lancet. 2024;404(10464):1761–78.
2. Riazi K, Azhari H, Charette JH, et al. The prevalence and incidence of NAFLD worldwide: a systematic review and meta-analysis. The Lancet Gastroenterology & Hepatology. 2022;7(9):851–61.
3. Schattenberg JM, Allen AM, Jarvis H, et al. A multistakeholder approach to innovations in NAFLD care. Commun Med (Lond). 2023;3(1):1.
4. Buzzetti E, Pinzani M. The multiple-hit pathogenesis of non-alcoholic fatty liver disease (NAFLD). Metab Clin Exp. 2016;65(8):1038–48.
5. Tacke F, Horn P, Wai-Sun Wong V, et al. EASL–EASD–EASO clinical practice guidelines on the management of metabolic dysfunction-associated steatotic liver disease (MASLD). J Hepatol. 2024;81(3):492–542.
6. Portincasa P, Khalil M, Mahdi L, et al. Metabolic dysfunction–associated steatotic liver disease: from pathogenesis to current therapeutic options. Int J Mol Sci. 2024;25(11):5640.
7. Zuo R, Ye L-F, Huang Y, et al. Hepatic small extracellular vesicles promote microvascular endothelial hyperpermeability during NAFLD via novel-miRNA-7. J Nanobiotechnol. 2021;19(1):396.
8. Zhu M, Jia Z, Yan X, et al. Danhe granule ameliorates nonalcoholic steatohepatitis and fibrosis in rats by inhibiting ceramide de novo synthesis related to CerS6 and CerK. J Ethnopharmacol. 2022;295:115427.
9. Graffmann N, Ring S, Kawala M-A, et al. Modeling nonalcoholic fatty liver disease with human pluripotent stem cell-derived immature hepatocyte-like cells reveals activation of PLIN2 and confirms regulatory functions of peroxisome proliferator-activated receptor alpha. Stem Cells Dev. 2016;25(15):1119–33.
10. Kang SWS, Fu D. Bioenergetics for hepatocyte polarization: coordination of multiple cellular organelles and the master regulator AMPK. Crit Rev Eukaryot Gene Expr. 2019;29(5):483–97.
11. Gissen P, Arias IM. Structural and functional hepatocyte polarity and liver disease. J Hepatol. 2015;63(4):1023–37.
12. Khamphaya T, Chukijrungroat N. Nonalcoholic fatty liver disease impairs expression of the type II inositol 1,4,5-trisphosphate receptor. Hepatology. 2018;67(2):560–74.
13. Michaut A, Le Guillou D, Moreau C, et al. A cellular model to study drug-induced liver injury in nonalcoholic fatty liver disease: application to acetaminophen. Toxicol Appl Pharmacol. 2016;292:40–55.
14. Parafati M, Kirby RJ, Khorasanizadeh S, et al. A nonalcoholic fatty liver disease model in human induced pluripotent stem cell-derived hepatocytes, created by endoplasmic reticulum stress-induced steatosis. Dis Model Mech. 2018;11(9):dmm033530.

15. Sinton MC, Meseguer-Ripolles J, Lucendo-Villarin B, et al. A human pluripotent stem cell model for the analysis of metabolic dysfunction in hepatic steatosis. iScience. 2021;24(1): 101931.
16. Pingitore P, Sasidharan K, Ekstrand M, et al. Human multilineage 3D spheroids as a model of liver steatosis and fibrosis. Int J Mol Sci. 2019;20(7):1629.
17. Wang J, Situ P, Chen S, et al. Hepatic polarized differentiation promoted the maturity and liver function of human embryonic stem cell-derived hepatocytes via activating Hippo and AMPK signaling pathways. Cells. 2022;11(24):4117.
18. Zeigerer A, Wuttke A, Marsico G, et al. Functional properties of hepatocytes in vitro are correlated with cell polarity maintenance. Exp Cell Res. 2017;350(1):242–52.
19. Vosough M, Omidinia E, Kadivar M, et al. Generation of functional hepatocyte-like cells from human pluripotent stem cells in a scalable suspension culture. Stem Cells Dev. 2013;22(20):2693–705.
20. Hendriks D, Brouwers JF, Hamer K, et al. Engineered human hepatocyte organoids enable CRISPR-based target discovery and drug screening for steatosis. Nat Biotechnol. 2023;41(11):1567–81.
21. Hendriks D, Artegiani B, Margaritis T, et al. Mapping of mitogen and metabolic sensitivity in organoids defines requirements for human hepatocyte growth. Nat Commun. 2024;15(1):4034.
22. Weng Y, Han S, Sekyi MT, et al. Self-assembled Matrigel-Free iPSC-Derived liver organoids demonstrate wide-ranging highly differentiated liver functions. Stem Cells. 2023;41(2):126–39.
23. Yamashita T, Takayama K, Sakurai F, et al. Billion-scale production of hepatocyte-like cells from human induced pluripotent stem cells. Biochem Biophys Res Commun. 2018;496(4):1269–75.
24. Wu H, Wang J, Liu S, et al. Large-Scale production of expandable hepatoblast organoids and polarised hepatocyte organoids from hESCs under 3D static and dynamic suspension conditions. Cell Prolif. 2025;0:e70001.
25. Ramli MNB, Lim YS, Koe CT, et al. Human pluripotent stem Cell-Derived organoids as models of liver disease. Gastroenterology. 2020;159(4):1471-e8612.
26. Podszun MC, Alawad AS, Lingala S, et al. Vitamin E treatment in NAFLD patients demonstrates that oxidative stress drives steatosis through upregulation of de-novo lipogenesis. Redox Biol. 2020;37:101710.
27. Seo SH, Lee DH, Lee YS, et al. Co-administration of ursodeoxycholic acid with rosuvastatin/ezetimibe in a non-alcoholic fatty liver disease model. Gastroenterol Rep. 2022;10:goac037.
28. Li T, Fang T, Xu L, et al. Empagliflozin alleviates hepatic steatosis by activating the AMPK-TET2-Autophagy pathway in vivo and in vitro. Front Pharmacol. 2021;16:1478437.
29. Zhou Y, Zhang L, Ma Y, et al. Secretome of senescent hepatic stellate cells favors malignant transformation from nonalcoholic steatohepatitis-fibrotic progression to hepatocellular carcinoma. Theranostics. 2023;13(13):4430–48.
30. Wang L, Li M, Yu B, et al. Recapitulating lipid accumulation and related metabolic dysregulation in human liver-derived organoids. J Mol Med. 2022;100(3):471–84.
31. Wesley BT, Ross ADB, Muraro D, et al. Single-cell atlas of human liver development reveals pathways directing hepatic cell fates. Nat Cell Biol. 2022;24(10):1487–98.
32. Halpern KB, Shenhav R, Matcovitch-Natan O, et al. Single-cell spatial reconstruction reveals global division of labour in the mammalian liver. Nature. 2017;542(7641):352–6.
33. Macparland SA, Liu JC, Ma X-Z, et al. Single cell RNA sequencing of human liver reveals distinct intrahepatic macrophage populations. Nat Commun. 2018;9(1):4383.
34. Hu H, Gehart H. Long-term expansion of functional mouse and human hepatocytes as 3D organoids. Cell. 2018;175(6):1591-606.e19.
35. Lyall MJ, Cartier J, Thomson JP, et al. Modelling non-alcoholic fatty liver disease in human hepatocyte-like cells. Philos Trans R Soc Lond B Biol Sci. 2018;373(1750):20170362.
36. Schönfeld P. Fatty acids as modulators of the cellular production of reactive oxygen species. Free Radic Biol Med. 2008;45(3):231–41.
37. Saber SH, Yak N, Yong XLH, et al. DDHD2 provides a flux of saturated fatty acids for neuronal energy and function. Nat Metab. 2025;7(10):2117–41.

Publisher's note

Springer Nature remains neutral with regard to jurisdictional claims in published maps and institutional affiliations.